

The Effect of Preaging Deformation on the Precipitation Behavior of an Al-Mg-Si Alloy

KATHARINA TEICHMANN, CALIN D. MARIOARA, SIGMUND J. ANDERSEN,
and KNUT MARTHINSEN

Transmission electron microscopy (TEM) studies were performed on an undeformed and a 10 pct predeformed condition of a commercial Al-Mg-Si alloy (AA6060) to investigate the effect of deformation prior to aging 300 minutes at 463 K (190 °C) on precipitate microstructure and precipitate types. Homogeneous precipitation of β'' -type precipitates, many of them disordered, was observed in the undeformed condition. Heterogeneous precipitation was found in the predeformed condition with fewer, coarser precipitates nucleated on dislocation lines producing a higher volume fraction compared with the undeformed condition. The precipitation sequence changed in the presence of dislocations, with most precipitates in the predeformed material being of post- β'' type. These microstructure findings were correlated with the tensile strength properties of the material. For the tensile tests, the undeformed and 10 pct predeformed materials were subsequently aged at 463 K (190 °C) for 0, 10, 100, and 300 minutes before testing at room temperature. The results show that the yield strength of the tested conditions was higher with predeformation for all aging times despite the relatively lower contribution of the precipitates to the total yield strength. Furthermore, it was shown that the maximum yield strength was reached for the predeformed material after shorter annealing times.

DOI: 10.1007/s11661-012-1235-0

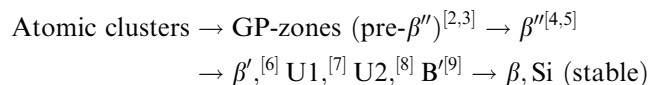
© The Minerals, Metals & Materials Society and ASM International 2012

I. INTRODUCTION

AL-MG-SI(-CU) alloys are an important class of materials for structural applications and are the most commonly extruded alloys. The reasons behind are the good combination of properties, such as high strength/weight ratio for stiffer, lighter constructions; good ductility, formability, and weldability; and good corrosion resistance.

The material properties are a result of microstructure characteristics. As Al-Mg-Si alloys are heat treatable, they gain their strength mainly through the formation of metastable nanometer-scaled precipitates during aging. Generally, fine and homogeneous precipitate microstructures give superior material properties. Optimization of the material properties is achieved through the control of precipitate formation with respect to type, size, distribution, number density, and volume fraction, by manipulating alloy composition and thermomechanical processing. Microstructure characterization and quantification is therefore important for industrial alloy design, and it aids the fundamental understanding of these alloys.

The precipitation sequence in undeformed Al-Mg-Si alloys is generally accepted to be^[1]



All metastable precipitates in this system have needle/lath/rod morphologies with longest dimension oriented along (001) Al directions, in which they are fully coherent with the aluminum matrix.

At peak hardness conditions, a microstructure exists with very fine GP-zones and β'' precipitates.^[2,10] The coarser post- β'' phases, namely β' , U1, U2, and B' (the last three also called type A, B, and C, respectively^[11]) generally appear after overaging, associated with a decrease in material hardness.^[1]

All metastable phases in the Al-Mg-Si(-Cu) system, including the disordered precipitates, are structurally related through a common network consisting of Si atomic columns with a projected near-hexagonal subcell (SC) $a = b \approx 0.4$ nm, $c = n \cdot 0.405$ nm, n being an integer, as shown by Andersen *et al.*^[7,12-14] The hexagonal c -axis of the network is parallel with the longest dimension of the precipitate. The Si network's SC deviates most from a hexagonal symmetry in the case of the pre- β'' and β'' phases, probably because of their high coherency with the Al matrix.

After extrusion, many products made of age-hardening Al alloys are subjected to different forms of deformation before the aging heat treatment takes place. Even without subsequent forming, extruded profiles often have to be stretched to straighten out a certain degree of bending and buckling after the extrusion. In this case, the formation of precipitates takes place in a material

KATHARINA TEICHMANN, PhD Student, and KNUT MARTHINSEN, Professor, are with the Norwegian University of Science and Technology, Trondheim 7491, Norway. Contact e-mail: katharina.teichmann@material.ntnu.no CALIN D. MARIOARA and SIGMUND J. ANDERSEN, Scientists, are with SINTEF Materials and Chemistry, Trondheim 7465, Norway.

Manuscript submitted October 18, 2011.

Article published online May 31, 2012

deformed to various degrees. The introduced dislocations then provide heterogeneous nucleation sites that may change the precipitation kinetics and the precipitation sequence.

Accelerated precipitation kinetics following deformation was observed by Genevois *et al.*^[15] in an AA2024 alloy. Deschamps *et al.*^[16] reported on a change in the precipitation sequence in a predeformed Al-Zn-Mg alloy: They showed that the stable phase was precipitated at the dislocations.

Matsuda *et al.*^[17,18] showed that in the presence of dislocations, a string-like phase, together with an elongated type and type C (B') precipitates, are formed on the dislocations. Yassar *et al.*^[19] investigated the precipitation of metastable phases of an AA6022 alloy during differential scanning calorimetry experiments by transmission electron microscopy (TEM). Although this result does not necessarily reflect isothermal precipitation behavior, it was shown that in the presence of dislocations the β'' -phase is not formed.

Because of the technological importance of deformed materials, this study gives a detailed investigation of the effect of 10 pct preaging deformation in a commercial Al-Mg-Si alloy (AA6060), with respect to distribution, microstructure, and type of the precipitates formed. The corresponding room-temperature tensile strength properties in different conditions, *i.e.*, without and with 10 pct predeformation and after different aging times (*i.e.*, 0, 10, 100, and 300 minutes at 463 K [190 °C]), have been analyzed and are discussed in view of the microstructure findings.

II. EXPERIMENTAL

For all experiments, an AA6060 alloy was used. Its composition is shown in Table I.

The material was initially machined into round tensile test samples with the geometry shown in Figure 1. Two conditions were prepared for TEM investigations. For both conditions, the tensile test samples were first solution heat treated in a salt bath at 818 K (545 °C) for 5 minutes and then water quenched. Within 30 minutes at room temperature, some of the samples were plastically deformed to 10 pct, whereas the others were left undeformed. All samples were further annealed at 463 K (190 °C) for 300 minutes (corresponding to a near-peak-aged condition in this alloy), thus creating one undeformed and one predeformed condition.^[20] In addition, other conditions corresponding to undeformed and 10 pct predeformed cases were annealed at 463 K (190 °C) for 0, 10, and 100 minutes to determine the (tensile) strength evolution during the isothermal heat treatment and to separate the strength contribution of precipitates from that of the solid solution and introduced dislocations.

TEM specimens were prepared by first cutting in the transversal direction 1.5-mm-long disks from the middle of the tensile test samples. These disks were then mechanically ground to a thickness of around 100 μm . To reach thicknesses suitable for electron transparency in TEM, the samples were electropolished with a Tenupol-3 machine (Struers Inc., Cleveland, OH). The electrolyte consisted of 1/3 HNO_3 and 2/3 methanol. The electrolyte temperature was kept at approximately 245 K (−28 °C). Four microscopes were used for the investigations: JEOL JEM-2010 and JEOL JEM-2010F operated at 200 kV (JEOL Ltd., Tokyo, Japan), a Philips CM30 operated at 150 kV (Philips, Amsterdam, the Netherlands), and a probe Cs-corrected FEI Titan 80-300ST TEM/scanning TEM (STEM) operated at 300 kV (FEI Corporation, Hillsboro, OR).

Measurements of average needle lengths, cross sections, precipitate number densities, and volume fractions were performed on TEM film negatives acquired with the Philips CM30 microscope in bright-field mode. A Gatan parallel electron energy loss spectrometer (Gatan, Inc., Pleasanton, CA) was used to determine specimen thickness, necessary for the precipitate quantification procedure. Details about the method can be found elsewhere.^[21] The JEOL JEM-2010F and JEOL JEM-2010 microscopes were used in high-resolution TEM (HRTEM) mode for precipitate crystal structure identification, whereas the Cs-corrected FEI Titan was used for the same purpose in high-angle annular dark-field STEM (HAADF-STEM) mode. The point resolution of the JEOL JEM-2010F microscope was 0.2 nm. For the HAADF-STEM image acquisition, a 50 mrad collector angle and nominal 0.08 nm probe size were used. The use of aberration-corrected HAADF-STEM over the HRTEM technique has many advantages: In addition to a spatial resolution toward 0.1 nm, the images contain Z-contrast and are more directly interpretable, being less affected by small changes in objective lens defocus and specimen thickness.^[22] The main disadvantages with HAADF-STEM are image distortions caused by specimen drift during the electron-scan and low signal-to-noise ratios in recorded images.

Because of the specific precipitate orientation with respect to the Al matrix, for thin specimens oriented in an $\langle 001 \rangle_{\text{Al}}$ zone, 1/3 of the precipitates will be viewed in cross section along their longest dimension, many without Al overlap. This enables the measurement of average precipitate cross sections and the visualization

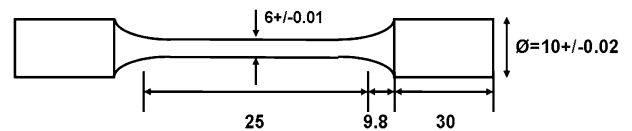


Fig. 1—Sample geometry and dimensions (mm).

Table I. Composition of the Investigated Alloy, in Weight Percent

Alloy	Al	Mg	Si	Mn	Fe	Ti	Cu	Zn	Cr
AA6060	balanced	0.47	0.41	0.02	0.2	0.008	0.003	0.009	0.002

of their crystal structures, making phase identification easier. The other 2/3 of precipitates will be viewed perpendicular to their longest dimension, enabling the measurement of their average length. For these reasons, all TEM images shown in this work correspond to specimens oriented in a $\langle 001 \rangle$ Al zone.

The tensile properties were measured at room temperature on all conditions (with and without predeformation). A hydraulic MTS 810 testing machine was used with a constant crosshead speed of 2 mm/min, corresponding to a strain rate of $1.3 \times 10^{-3} \text{ s}^{-1}$. To assure the accuracy of the measurements, each condition was tested with three samples. The tensile direction was parallel to the extrusion direction.

III. RESULTS AND DISCUSSION

Predeformation before the aging heat treatment leads to a different microstructure of the material compared with the undeformed condition, as can be observed in Figure 2 and Table II. In Figure 2 (left), an overview of the undeformed material reveals a homogeneous precipitate distribution. On the contrary, the overview in Figure 2 (right) of the predeformed material clearly shows an inhomogeneous distribution of larger precipitates nucleated along dislocation lines.

The microstructure quantification in Table II shows that the precipitates formed in the dislocation-containing predeformed material are fewer, coarser, and yield a higher volume fraction than in the undeformed material.

For a more in-depth characterization of the microstructure, HRTEM and aberration corrected HAADF-STEM was performed to determine the type of the precipitates formed during the heat treatment. Representative precipitates from the undeformed and the predeformed conditions are presented in Figures 3 through 6. Table III shows statistics for the dominant precipitate-types occurring in the two investigated conditions.

Most of the analyzed precipitates in the undeformed material were found to contain various degrees of disorder. The most common symmetry observed was consistent with the β'' phase. However, a significant fraction of precipitates also showed post- β'' symmetries (Table III), characterized by a more hexagonal configuration of the Si-network.^[7,10,14] Examples of precipitates from this condition are shown by HRTEM images in Figure 3 and by HAADF-STEM images in Figure 4. The precipitates in Figure 3 can be explained as disordered β'' (Figure 3(a)) and disordered β' (Figure 3(c)). Figure 4(a) shows a disordered β'' -precipitate, whereas a combination of β' and U2 phases in one precipitate is observed in Figure 4(c). Because of the superior spatial resolution, high accuracy in the projected positions of each atomic column is achieved for the precipitates in Figure 4, whereas the Z-contrast information enables identification of most Si columns. The complexity of such disordered precipitates requires subsequent analysis of the HAADF-STEM images to understand more completely the interconnection of different precipitate internal parts, the stability of the Si-network, and the precipitate-matrix interfaces. It is interesting to mention that a mixture of different phases in one precipitate has been observed previously.^[8] In all cases, the transition between the phases is smooth, without obvious internal interfaces.

Table II. Microstructure Parameters in the Undeformed and 10 pct Predeformed Materials Followed by 300 Min Heat Treatment at 463 K (190 °C)

Parameter	Undeformed	10 pct Predeformed
$\langle l \rangle$ (nm)	41.64 to 44.09	116.12 to 129.32
$\langle CS \rangle$ (nm ²)	8.58 to 9.22	25.06 to 28.26
$\langle \rho \rangle$ (needles/ μm^3)	10733 to 12675	2027 to 2296
$\langle VF \rangle$ (pct)	0.42 to 0.50	0.62 to 0.80

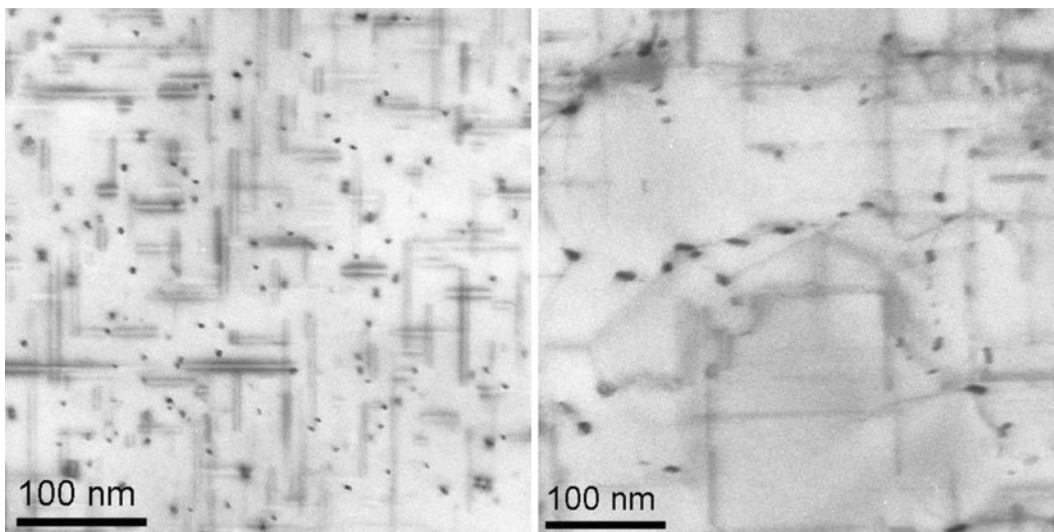


Fig. 2—Overview of the microstructure in AA6060 after 300 min heat treatment at 463 K (190 °C): undeformed (left) and 10 pct predeformed (right).

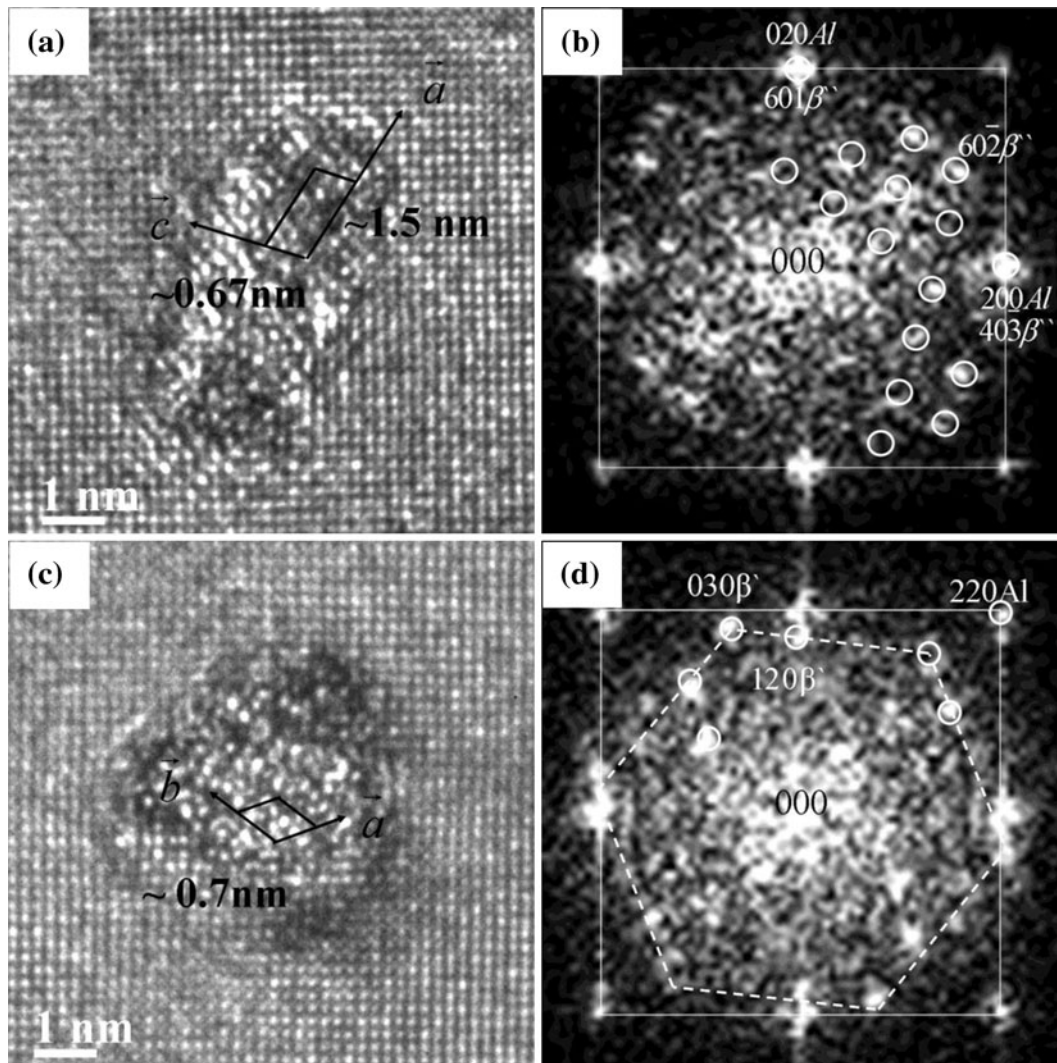


Fig. 3—HRTEM images of precipitate types in the undeformed AA6060 after 300 min annealing at 463 K (190 °C). (a) Disordered β'' with marked unit cell. (b) Fast Fourier transform (FFT) of (a) where full circles indicate spots corresponding to β'' symmetry. (c) Disordered β' with marked unit cell. (d) FFT of (c). Full circles indicate spots corresponding to β' symmetry. Spots corresponding to the hexagonal Si-network are connected by dashed lines. In all FFT patterns, the Al matrix spots are connected by thin continuous lines.

The observed disorder in the undeformed condition indicates that after 300 minutes at 463 K (190 °C), the precipitates are already overaging and in a transition state from β'' to post- β'' phases.

All investigated Al-Mg-Si precipitates located at grain boundaries were of B'-type, with one example shown in Figure 5. These precipitates are of a much larger size than the precipitates formed within the matrix.

Although disorder was also found in the precipitates nucleated along dislocation lines in the predeformed material, most of them had symmetries consistent with post- β'' -type phases. Figure 6 shows examples of such precipitates: disordered B' (Figure 6(a)), disordered U2 precipitate (Figure 6(c)), and mixed $\beta'/$ U2 precipitate (Figure 6(e)).

From Table III, it can be observed that the percentage of β'' is greatly reduced in the predeformed condition, indicating that dislocations serve as heterogeneous nucleation sites that favor a direct precipitation

of post- β'' phases. This conclusion is strengthened by previous results showing that, for the same alloy, no β'' phase was observed in a 10 pct predeformed material followed by 10 minutes aging at 463 K (190 °C).^[23]

The microstructural changes can largely be understood by the observations made by Embury and Nicholson^[24] and Lorimer and Nicholson.^[25] This work shows that dislocations influence the precipitation in two different ways: First, they provide heterogeneous nucleation sites, and second, they absorb excess vacancies from the matrix leaving an area behind with a lower vacancy concentration, which might make it more difficult to form GP zones responsible for a homogeneous distribution of nuclei for β'' -precipitates during the following heat treatment. Furthermore, solute atoms might segregate at the dislocation creating a solute-depleted area around the dislocations. These observations are confirmed in the current work by the observation of an inhomogeneous distribution of post- β''

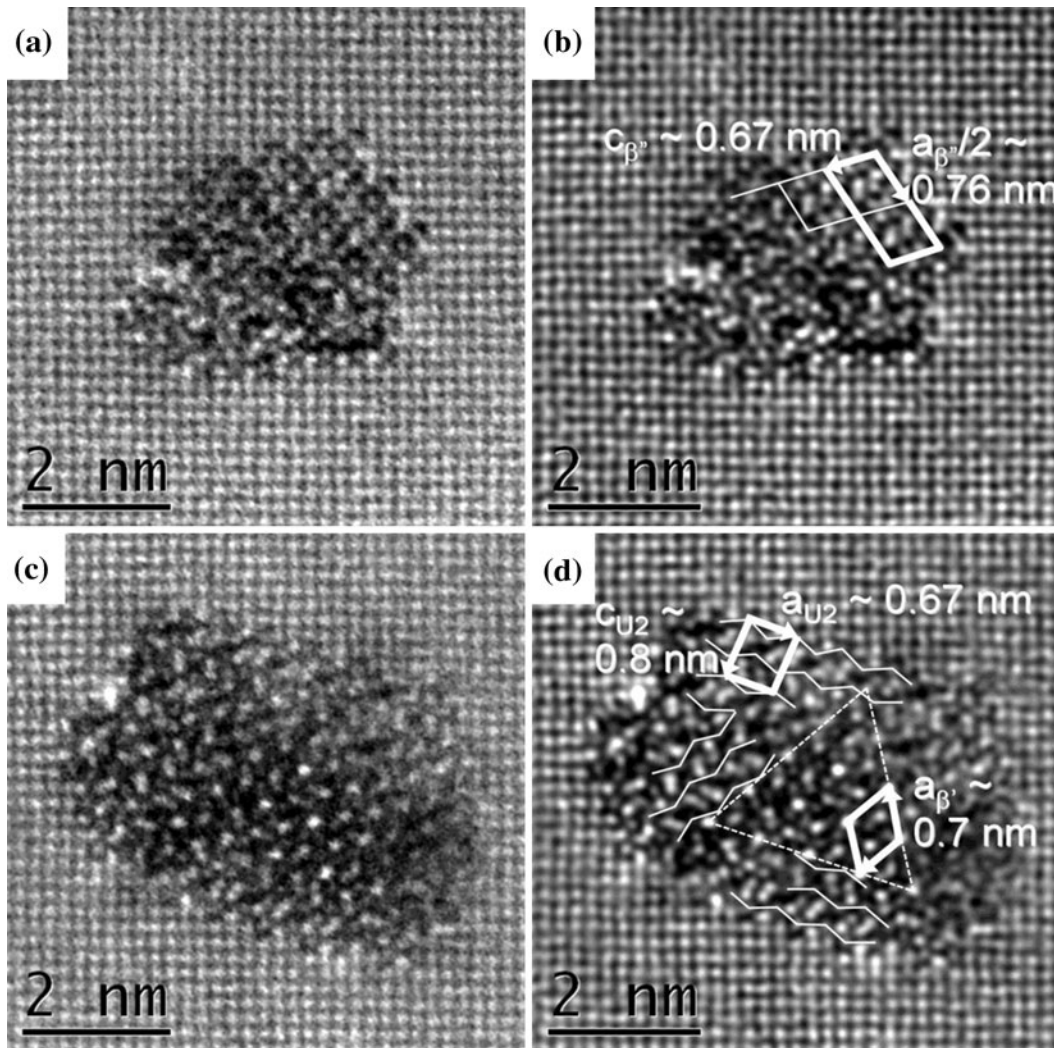


Fig. 4—HAADF-STEM images of precipitate types in the undeformed AA6060 after 300 min annealing at 463 K (190 °C). (a) Raw image of a disordered β'' . (b) To reduce noise, a Fourier filter was applied by using a circular band-pass mask that removed all distances shorter than 0.14 nm in the original image (a). The β'' part is indicated by continuous lines that connect the (origin) Mg1 atomic columns in the phase's crystal structure.^[4] One β'' unit cell is shown with thick lines. (c) Raw image of a disordered precipitate that contains domains consistent with β' and U2 phases. (d) Fourier filtered image of (c), with filtering performed in the same manner as in (b). The β' part is delimited by dashed lines that connect Si columns.^[6] The U2 parts are indicated by wavy lines that connect Mg columns along [100]U2 ($a = 0.67$ nm).^[8] One unit cell for each phase is shown with thick lines.

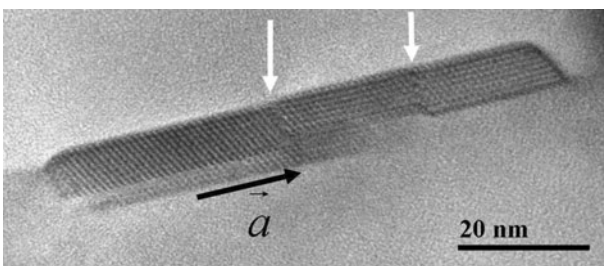


Fig. 5—Grain boundary precipitate in the undeformed material. Measurement of unit cell parameters and symmetry identifies it as hexagonal B' type. One hexagonal plane base $\langle 100 \rangle B'$ ($a = 1.04$ nm), indicated by the black arrow, is directed along the grain boundary. The precipitate is observed to contain internal faults; see the white arrows.

precipitates in the deformed material. The coarser sizes of the precipitates are in accordance with previous studies on grain boundary and dislocation-grown precipitates. In a material with dislocations, the coarsening depends on the diffusion of solute along the dislocation.^[26]

The microstructure characteristics of the two analyzed conditions are in the following correlated with the corresponding tensile strength properties. Figure 7 shows the true stress-strain curves for the undeformed and the 10 pct predeformed materials after aging for 0, 10, 100, and 300 minutes at 463 K (190 °C), respectively.

The total yield strength and maximum strength may be considered to consist of three individual contributions

$$\sigma_{\text{total}} = \Delta\sigma_{\text{ss}} + \Delta\sigma_{\text{d}} + \Delta\sigma_{\text{p}}$$

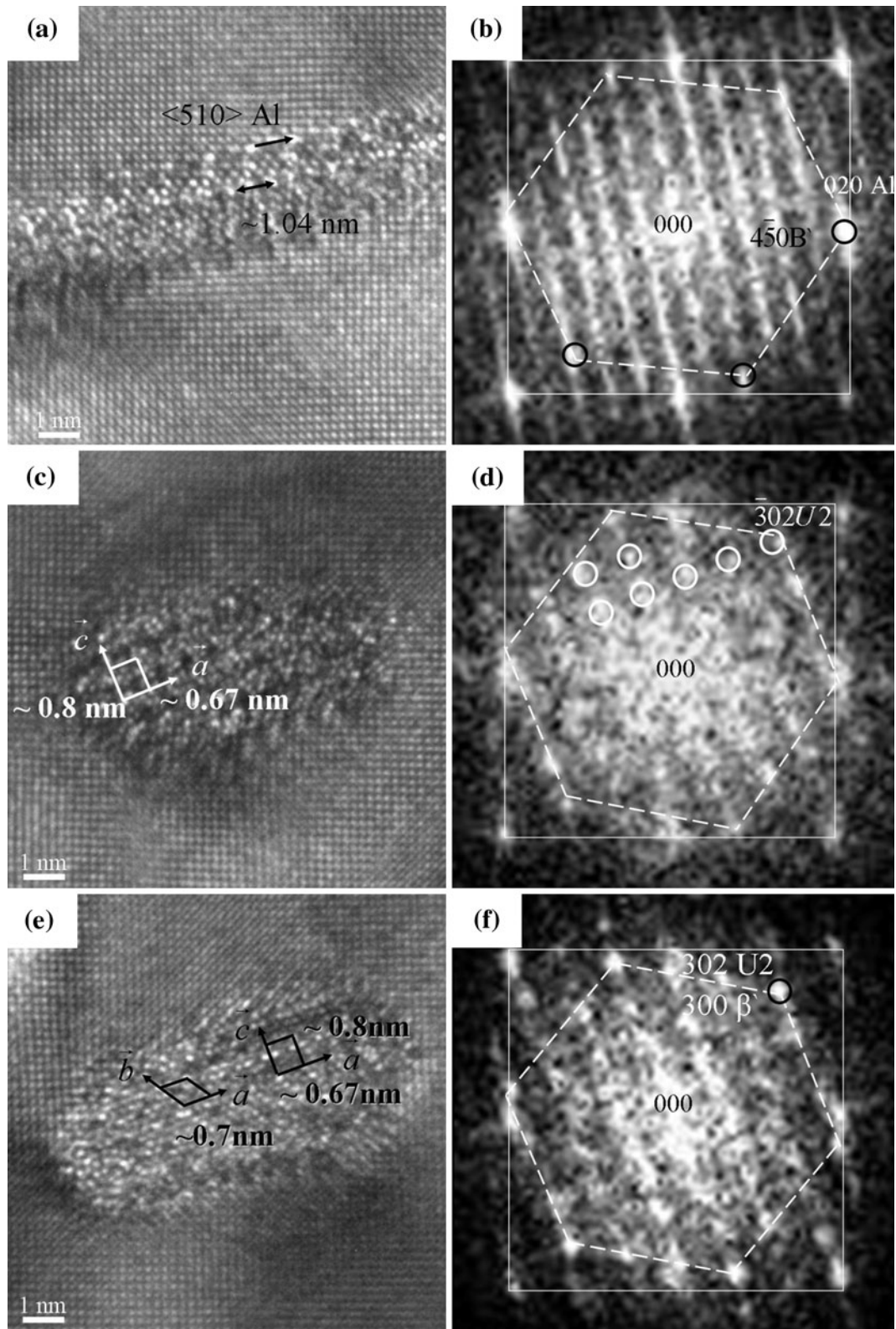


Fig. 6—Precipitate types in the 10 pct preformed AA6060 after 300 min annealing at 463 K (190 °C). (a) B' like precipitate with the marked periodicity of 1.04 nm along $\langle 510 \rangle \text{Al}$ (b) FFT of (a). Spots marked by full circles are indexed according to B' symmetry and are also generated by the Si-network substructure. (c) Disordered U2, with marked unit cell. (d) FFT of (c) where spots corresponding to the U2 symmetry are indicated by full circles. (e) Precipitate consisting of β' in the lower left part of the precipitate and U2 in the upper right part of the precipitate with the unit cells marked. (f) FFT of (e) with one indexed spot that corresponds to both β' and U2 phases, as well as to their common Si-network. In all FFT patterns, the Al matrix spots are connected by thin continuous lines and the Si-network spots are connected by dashed lines. The B', U2, and β' phases have the same orientation of their Si-networks with respect to the Al matrix,^[7,12–14] also demonstrated by their FFT patterns (see also Figs. 3(c) and (d)).

with $\Delta\sigma_{ss}$ being the solid-solution strength addition, $\Delta\sigma_d$ the dislocation strength addition, and $\Delta\sigma_p$ the precipitate strength addition. The solid-solution strength addition $\Delta\sigma_{ss}$ was estimated by taking the yield stress of the undeformed and not annealed sample 0 pct_0 minutes, whereas the contribution of $\Delta\sigma_d$ was estimated by taking the difference between the true stress at 10 pct strain and the yield stress σ_y of the same material condition. Table IV shows the relative strength additions for all different conditions. The strength addition by clusters

Table III. Precipitate Statistics for the Undeformed and 10 pct Predeformed Samples of AA6060 After Annealing 300 Min at 463 K (190 °C)*

Precipitate Symmetry [pct]	Undeformed	10 pct Predeformed
β'' type	58	3
post- β'' type	42	97

*The total number of analyzed precipitates in the undeformed material was 52, and in the predeformed material 59, ensuring satisfactory statistics^[21] and reliable qualitative conclusions.

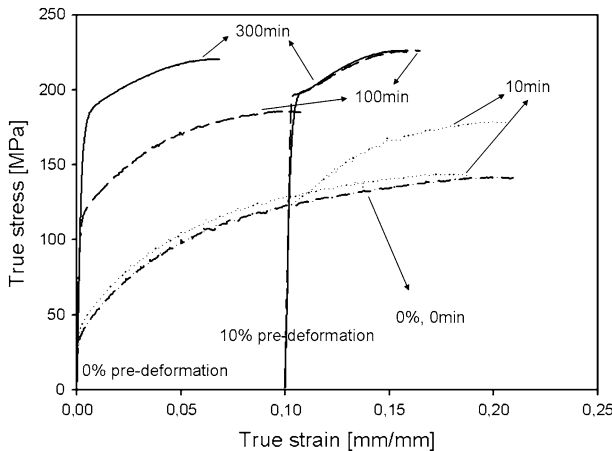


Fig. 7—Tensile strength properties acquired at room temperature from undeformed and 10 pct predeformed materials that were further heat treated at 463 K (190 °C) for 0, 10, 100, and 300 mins. The curves corresponding to 10 pct predeformation are shifted along the x-axis according to the predeformation.

forming during room-temperature storage has been tested and was found to be negligible both for the undeformed (≈ 0 MPa) and the deformed material (≈ 1 MPa). The contribution of the dislocations was assumed to be constant during the subsequent heat treatment. Recovery as a result of dislocation annihilation has thus been neglected. This assumption has been verified by redoing all the experiments with a non-heat-treatable 5xxx type alloy, namely Al-Mg 1 pct. This alloy has a similar solute concentration as the used Al-Mg-Si alloy but does not form any precipitates during heat treatment. The acquired yield strength after different thermomechanical treatments can just be assumed to be solely caused by solute solution and dislocation strengthening. Both the solid-solution strengthening addition and the dislocation strengthening without heat treatment were very similar to the used 6060 alloy, and thus, the two alloys are comparable. The yield strength was observed to be almost constant during the heat treatment. More detailed experiments showed that the $\Delta\sigma_{ss}$ contribution stayed also almost constant during the heat treatment of 10 minutes and 300 minutes, and consequently, so did the $\Delta\sigma_d$ contribution, which was observed to change by a maximum of 8 pct. To be sure that the conclusions from Table IV hold, the $\Delta\sigma_d$ contribution was changed as an extreme by 20 pct for the case of the 6060 alloy, leading to the same conclusions. The reason for an almost constant dislocation density might be the clustering of the solute elements at the dislocation core, which would lead to a dislocation pinning and thus to a reduced dislocation annihilation. A dislocation-solute interaction of this kind has been reported earlier.^[27]

In contrast to the tensile test curves of the undeformed material, the predeformed conditions show indications of a plateau after yielding as it can be observed in Figure 7. This apparent yield phenomenon is likely caused by an extra stress needed to unpin the dislocations that had been introduced during the predeformation and that were pinned by the precipitates forming during the annealing. When these dislocations become free to move, the stress drops.

It can be observed that the relative strength addition of precipitation decreases drastically after predeformation of the material and that the yield strength in this case is largely determined through dislocation

Table IV. Relative Strength Additions to the Yield Strength of the Different Conditions*

	Yield Strength (MPa)	$\Delta\sigma_{ss}$ (MPa)	$\Delta\sigma_d$ (MPa)	$\Delta\sigma_p$ (MPa)	Relative Strength Addition of Precipitates (pct)
0 pct_0 min	30	30	—	—	—
0 pct_10 min	40	30	—	10	25
0 pct_100 min	110	30	—	80	73 (100)
0 pct_300 min	180	30	—	150	83 (100)
10 pct_10 min	120	30	90	0	0
10 pct_100 min	192	30	90	72	37 (53)
10 pct_300 min	195	30	90	75	38 (54)

*The value of $\Delta\sigma_{ss}$ is for simplicity reasons kept constant for all conditions, although the strength contribution from the solid solution must decrease during aging because of precipitation. Therefore, the numbers in parentheses show the relative strength addition of precipitates if the solid-solution strength addition, in the most extreme case, is considered zero for these conditions.

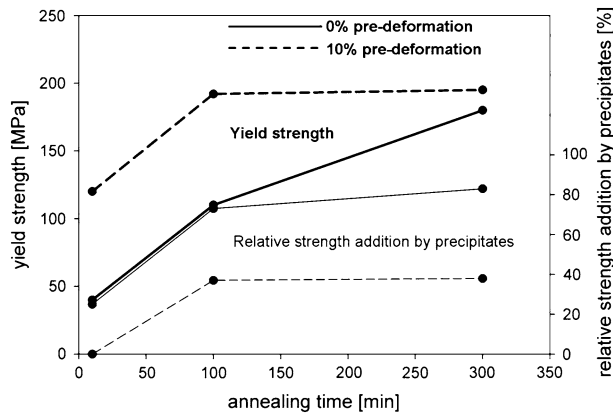


Fig. 8—Evolution of yield strength (left axis) and the relative contribution by the precipitates to the yield strength (right axis) as a function of annealing time.

hardening. Figure 8 shows the evolution of yield strength and of relative strength contribution by the precipitates to the yield strength. The yield strength is higher for all annealing times and is reached faster in the 10 pct predeformed material. The lower relative strength contribution by the precipitates in the 10 pct predeformed material may be understood by the coarse microstructure and a low strengthening potential of the post- β'' type precipitates.^[1] The relative low yield strength of the 10 pct predeformed condition after 300 minutes is caused by the faster overaging in the deformed material. These findings are in agreement with work done by Kolar *et al.*,^[20] which provides a more detailed analysis of the tensile properties in similar Al-Mg-Si alloys.

IV. CONCLUSIONS

The results presented in this article clearly show that deforming a material prior to aging has a profound effect on the precipitation behavior. The introduced dislocations act as heterogeneous nucleation sites and fast diffusion paths, with the consequence that the precipitate microstructure, local distribution, and the precipitate type is altered.

The following differences have been observed between 10 pct predeformed and undeformed materials after aging at 463 K (190 °C):

1. In the predeformed material, the precipitation is inhomogeneous and takes place along the introduced dislocations. In the undeformed condition, a more homogeneous nucleation/spatial distribution of precipitates is observed.
2. The precipitates formed in the predeformed material are coarser, with a lower number density producing a higher volume fraction compared with the precipitates in the undeformed material.
3. The precipitate type changes from predominantly β'' in the undeformed condition to post- β'' in the predeformed condition.
4. The yield strength of the predeformed material is largely influenced by the dislocation strength

addition. The relative strength addition by precipitates is reduced because of the changed precipitation kinetics and thus different types of precipitates, *e.g.*, post- β'' -precipitates.

5. The maximum yield strength in the predeformed material is reached after shorter annealing times as compared to the undeformed material.

ACKNOWLEDGMENTS

Financial support was received from NTNU *via* the scholarship financing this thesis, and the Research Council of Norway provided funding *via* two projects: 177600/V30 “Fundamental investigations of solute clustering and nucleation of precipitation” and project 176816/I40 “Nucleation control for optimised properties,” which is also supported by Hydro and Steertec Raufoss AS. We would also like to thank Dr. C. Boothroyd at DTU, Denmark for the images in Figure 4 and Michal Kolar for his help with the sample preparation.

REFERENCES

1. C.D. Marioara, H. Nordmark, S.J. Andersen, and R. Holmestad: *J. Mater. Sci.*, 2006, vol. 41, pp. 471–78.
2. G.A. Edwards, K. Stiller, G.L. Dunlop, and M.J. Couper: *Acta Mater.*, 1998, vol. 46, pp. 3893–904.
3. C.D. Marioara, S.J. Andersen, J. Jansen, and H.W. Zandbergen: *Acta Mater.*, 2001, vol. 49, pp. 321–28.
4. S.J. Andersen, H.W. Zandbergen, J. Jansen, C. Traeholt, U. Tundal, and O. Reiso: *Acta Mater.*, 1998, vol. 46, pp. 3283–98.
5. H.S. Hasting, A.G. Frøseth, S.J. Andersen, R. Vissers, J.C. Walmsley, C.D. Marioara, F. Danoix, W. Lefebvre, and R. Holmestad: *J. Appl. Phys.*, 2009, vol. 106, pp. 123527-1–123527-9.
6. R. Vissers, M.A. van Huis, J. Jansen, H.W. Zandbergen, C.D. Marioara, and S.J. Andersen: *Acta Mater.*, 2007, vol. 55, pp. 3815–23.
7. S.J. Andersen, C.D. Marioara, R. Vissers, A. Frøseth, and H.W. Zandbergen: *Mater. Sci. Eng. A*, 2007, vol. 444, pp. 157–69.
8. S.J. Andersen, C.D. Marioara, A. Frøseth, R. Vissers, and H.W. Zandbergen: *Mater. Sci. Eng. A*, 2005, vol. 390, pp. 127–38.
9. R. Vissers, C.D. Marioara, S.J. Andersen, and R. Holmestad: *Aluminium Alloys*, 2008, vol. 2, pp. 1263–69.
10. W.F. Miao and D.E. Laughlin: *Scripta Mater.*, 1999, vol. 40, pp. 873–78.
11. K. Matsuda, Y. Sakaguchi, Y. Miyata, Y. Uetani, T. Sato, A. Kamio, and S. Ikeno: *J. Mater. Sci.*, 2000, vol. 35, pp. 179–89.
12. C.D. Marioara, S.J. Andersen, T.N. Stene, H. Hasting, J. Walmsley, A.T.J. Van Helvoort, and R. Holmestad: *Phil. Mag.*, 2007, vol. 87, pp. 3385–3413.
13. S.J. Andersen, C.D. Marioara, R. Vissers, A.L. Frøseth, and P. Derlet: *Proc. 13th European Microscopy Congress*, vol. 2, 2004, pp. 599–600.
14. S.J. Andersen, C.D. Marioara, R. Vissers, M. Torsæter, R. Bjørge, F.J.H. Ehlers, and R. Holmestad: *Mater. Sci. Forum*, 2010, vols. 638–642, pp. 390–95.
15. C. Genevois, D. Fabrègue, A. Deschamps, and W.J. Poole: *Mater. Sci. Eng. A*, 2006, vol. 441, pp. 39–48.
16. A. Deschamps, F. Livet, and Y. Bréchet: *Acta Mater.*, 1998, vol. 47, pp. 281–92.
17. K. Matsuda, H. Gamada, Y. Uetani, S. Rengakuji, F. Shinagawa, and S. Ikeno: *J.J.I.L.M.*, 1998, vol. 48, pp. 471–75.
18. K. Matsuda, S. Shimizu, H. Gamada, Y. Uetani, F. Shinagawa, and S. Ikeno: *J. Soc. Mater. Sci.*, 1999, vol. 48, pp. 10–15.
19. R.S. Yassar, D.P. Field, and H. Weiland: *Scripta Mater.*, 2005, vol. 53, pp. 299–303.
20. M. Kolar, K.O. Pedersen, S. Gulbrandsen-Dahl, K. Teichmann, and K. Marthinsen: *Metall. Mater. Trans. A*, 2011, vol. 52A, pp. 1356–62.

21. C.D. Marioara, S.J. Andersen, H.W. Zandbergen, and R. Holmestad: *Metall. Mater. Trans. A*, 2005, vol. 36A, pp. 691–702.
22. P.D. Nellist and S.J. Pennycook: *Ultramicroscopy*, 1999, vol. 78, pp. 111–24.
23. K. Teichmann, C.D. Marioara, S.J. Andersen, K.O. Pedersen, S. Gulbrandsen-Dahl, M. Kolar, R. Holmestad, and K. Marthinsen: *Phil Mag.*, 2011, vol. 91, pp. 3744–54.
24. J.D. Embury and R.B. Nicholson: *Acta Metall.*, 1965, vol. 13, pp. 403–17.
25. G.W. Lorimer and R.B. Nicholson: *Acta Metall.*, 1966, vol. 14, pp. 1009–13.
26. A.J. Ardell: *Acta Metall.*, 1972, vol. 20, pp. 601–09.
27. Z. Xu and R.C. Picu: *Modell. Simul. Mater. Sci. Eng.*, 2006, vol. 14, pp. 195–206.